

# Multi-scale Latent Point Consistency Models for 3D Shape Generation

Bi'an Du, *Student Member, IEEE*, Wei Hu, *Senior Member, IEEE*, and Renjie Liao

**Abstract**—Consistency Models (CMs) have significantly accelerated the sampling process in diffusion models, yielding impressive results in synthesizing high-resolution images. To explore and extend these advancements to point-cloud-based 3D shape generation, we propose a novel Multi-scale Latent Point Consistency Model (MLPCM). Our MLPCM follows a latent diffusion framework and introduces a hierarchy of latent representations, ranging from point-level to super-point levels, each corresponding to a different spatial resolution. We design a multi-scale latent integration module along with 3D spatial attention to effectively denoise the point-level latent representations conditioned on those from multiple super-point levels. Additionally, we propose a latent consistency model, learned through consistency distillation, that compresses the prior into a one-step generator. This significantly improves sampling efficiency while preserving the performance of the original teacher model. Extensive experiments on standard benchmarks ShapeNet and ShapeNet-Vol demonstrate that MLPCM achieves a 100x speedup in the generation process, while surpassing state-of-the-art diffusion models in terms of both shape quality and diversity.

**Index Terms**—Hierarchical latent space, 3D spacial attention, 3D point cloud generation, consistency models.

## I. INTRODUCTION

Generative modeling of 3D shapes plays a crucial role in various applications in 3D computer vision and graphics, empowering digital artists to create realistic and high-quality shapes [1, 2, 3, 4, 5, 6, 7]. For these models to be practically effective, they must provide flexibility for interactive refinement, support the synthesis of diverse shape variations, and generate smooth meshes that seamlessly integrate into standard graphics pipelines.

With the rapid advances in generative models for text, images, and videos, significant progress has also been made in 3D shape generation. Techniques based on variational autoencoders (VAEs) [8, 9, 10], generative adversarial networks (GANs) [11, 12, 13, 14], and normalizing flow models [2, 15, 16] have been proposed to generate 3D shapes. Recently, diffusion-based models [17] and their latent diffusion variants [3, 18] have achieved state-of-the-art results in this domain.

Despite notable progress, substantial obstacles remain when applying diffusion models to 3D shapes that are represented as point clouds. Point sets are unordered, irregular, and often highly non-uniform in density, which complicates both

neighborhood construction and feature aggregation [19, 20]. A single radius may fail to capture thin structures while a large radius may blur sharp edges, and k-nearest-neighbor graphs can become unstable under varying sampling density [20, 21]. Real data frequently contain noise, outliers, holes, and partial coverage from limited viewpoints [22, 23], so the denoiser must be robust to missing regions while still reconstructing fine details. In addition, 3D geometry introduces invariances and symmetries that are easy to violate. Models that are not carefully designed with respect to translation, rotation, and scale may overfit to coordinate frames or camera poses [24, 25]. These factors push the denoising network to learn representations that respect both local geometric primitives such as edges, corners, and small parts, and global object level regularities such as symmetry, topology, and part arrangement. Capturing these patterns jointly is essential for producing high quality point sets that are faithful at a small scale while remaining structurally coherent at a large scale.

A promising strategy is to diffuse in a learned latent space where shapes are summarized into compact codes that suppress nuisance variation and concentrate information about structure [3, 26]. Learning in latent space reduces computational cost and can improve stability, yet relying on a single level of latent representation has proved insufficient. A single scale cannot simultaneously preserve tiny geometric details and encode global layout, which leads to oversmoothed reconstructions or broken long range dependencies [27, 28]. Effective 3D generation therefore requires multiple levels or resolutions together with mechanisms that let information flow across them so that coarse latents guide overall structure while finer latents supply detail where needed [3]. A second challenge concerns practicality. The sampling process in diffusion models typically requires many iterative evaluations of the denoiser, which results in slow generation and high memory consumption [29]. Classifier free guidance and other conditioning signals further increase the computational burden [30]. Without acceleration, these costs hinder real world use in interactive modeling, editing, completion from sparse inputs, or deployment within larger 3D pipelines [31, 32]. Reducing the number of steps while preserving quality, for example through consistency distillation or higher order solvers in latent space [33, 34], remains critical for making diffusion-based point cloud generators both accurate and efficient.

Here we introduce Multi-scale Latent Point Consistency Models (MLPCM), a generative model for 3D shape synthesis that follows the latent diffusion paradigm while addressing the joint learning of fine local geometry and long range structural coherence within a single framework. The archi-

B. Du and W. Hu are with Wangxuan Institute of Computer Technology, Peking University, No. 128 Zhongguancun North Street, Beijing, China. E-mail: pkudba@stu.pku.edu.cn, forhuwei@pku.edu.cn

R. Liao is with Department of Electrical and Computer Engineering, University of British Columbia, Vancouver, Canada. E-mail: rjliao@ece.ubc.ca  
Corresponding author: Wei Hu.

texture is a hierarchical variational autoencoder that encodes each shape into multiple levels of latent variables, from point level to super-point levels, each aligned with a specific spatial resolution. These latents form an explicit hierarchy in the encoder so that information flows in both top down and bottom up directions. Coarse semantic latents provide guidance for the organization of global structure, while fine latents inject detail that refines and corrects coarse hypotheses. Diffusion operates on point level latents, which concentrates stochasticity where geometric detail resides and keeps higher level latents clean and semantically stable. A multi-scale latent integration module then conditions the denoiser by modulating noisy point latents with super-point latents from several scales. This cross-scale conditioning encourages the emergence of compositional regularities, supports reuse of part-level patterns across categories, and improves data efficiency under sparse or partial observations.

To further strengthen geometric fidelity and controllability, the denoising network integrates a 3D spatial attention mechanism whose bias term derives from pairwise Euclidean distances. This bias respects rigid transformations and encourages attention to concentrate on geometrically proximate regions while preserving the capacity to aggregate information across the entire shape when long range dependencies are beneficial. Training optimizes a hierarchical evidence lower bound for the VAE together with the standard latent diffusion objective. After training, consistency distillation in latent space yields a latent consistency model that preserves the visual quality of the diffusion sampler while reducing the number of refinement steps, which enables rapid sampling for interactive editing and conditional generation. In combination, hierarchical latent organization, multi-scale integration, geometry aware attention, and accelerated inference provide a practical foundation for downstream tasks such as completion from sparse views, structure-preserving editing, controllable synthesis with part level constraints, and conditional reconstruction from partial point clouds, while also improving robustness to noise, distribution shift, and limited supervision.

In summary, our main contributions are as follows:

- We propose a novel Multi-scale Latent Point Consistency Model for 3D shape generation, which builds a diffusion model with a hierarchical latent space, leveraging representations ranging from point to super-point levels.
- We propose a multi-scale latent integration module along with a 3D spatial attention mechanism to enable the denoiser to focus on salient neighbourhoods while maintaining global consistency, resulting in sharper topology and more uniform point distribution.
- We extend consistency distillation to unstructured point-latent spaces and couple it with multi-scale latent integration, yielding a student that inherits multi-scale semantics and generates 3D shapes in one to four steps without loss of visual or structural fidelity.
- Extensive experiments show that our method outperforms existing approaches on the widely used ShapeNet benchmark in terms of shape quality and diversity. Moreover, after consistency distillation, our model is 100x faster than the previous state-of-the-art in sampling.

## II. RELATED WORKS

In this section, we discuss related works on diffusion models, accelerating diffusion models and 3D point cloud generation, respectively.

### A. Diffusion Models

Diffusion models have achieved state-of-the-art results in image synthesis by learning to reverse a corruption process that gradually adds noise to data. In the common discrete-time formulation, the forward process is a fixed Markov chain that diffuses a clean sample into near-Gaussian noise, while the model is trained to predict either the noise or the score of the noised sample so that it can iteratively denoise at test time [29]. A complementary continuous-time view casts diffusion as stochastic differential equations and learns the score function of perturbed data, which unifies score-based generative modeling with diffusion under a single framework and enables alternative samplers [35, 36]. Maximum likelihood training for continuous-time score models further improves statistical efficiency and connects diffusion training to classic likelihood principles [37].

Scaling laws and architectural choices have made diffusion a robust default for high-fidelity image generation. Hierarchical or two-stage pipelines that combine powerful text encoders with diffusion backbones yield strong semantic control and photorealism [38, 39]. Learning the generative process in a compressed latent space rather than pixel space reduces computational burden and memory cost while maintaining visual quality, which has been key to high-resolution synthesis [26]. Compared with variational autoencoders and generative adversarial networks, diffusion models typically provide more stable optimization, reliable likelihood estimation, and improved mode coverage, mitigating common issues such as posterior collapse in VAEs and mode dropping in GANs [40, 41, 42]. During inference, samples are produced by integrating the learned reverse dynamics from noise toward data, which can be interpreted either as reversing a discrete diffusion chain or integrating an ODE or SDE defined by the learned score [29, 36].

### B. Accelerating Diffusion Models

Despite their success, diffusion models are constrained by slow sampling due to many iterative denoising steps. Training-free acceleration exploits the continuous-time formulation to integrate probability-flow ODE trajectories in fewer steps, including high-order solvers such as DPM-Solver and its improved variants, as well as unified predictor-corrector samplers and adaptive step-size schemes [32, 43, 44]. Training-based acceleration modifies objectives or adds light retraining to shorten trajectories: optimized discretization learns sampling times tailored to a fixed compute budget [45], truncated diffusion shortens the denoising horizon [46, 47], and neural-operator style learners amortize parts of the reverse dynamics [48]. Distillation compresses multi-step teachers into fast students by matching trajectories or terminal outputs, yielding few-step or even single-step generators [49, 50].

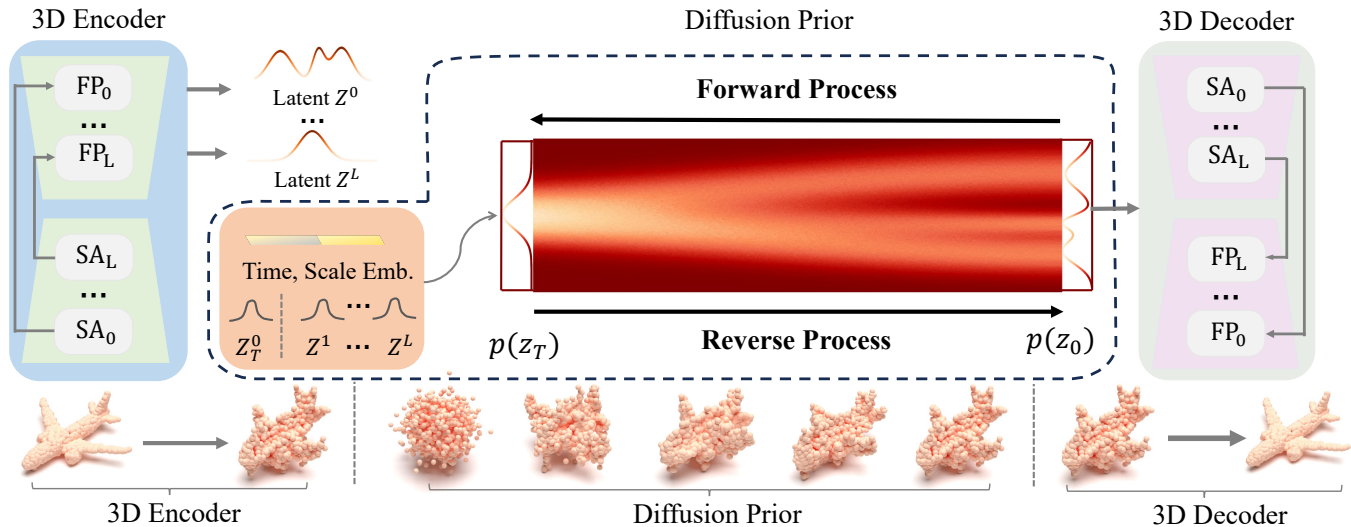


Fig. 1: An overview of the proposed multi-scale latent diffusion model. Hierarchical VAEs encode the input shape into latent variables at multiple resolutions, including point-level and super-point-level. Compared to the latent point diffusion model that only denoises the point-level latent space, our proposed multi-scale latent integration module injects higher-level latent variables to guide refinement, thereby jointly modeling local geometry and global structure. The details of the diffusion prior are shown in Figure 2.

Recent works push one-step and few-step generation further. Consistency Models enforce a mapping that is consistent along time and can be trained either by distillation or from scratch, enabling rapid one-step sampling [33]. Follow-up advances improve training stability and data-only training, reduce reliance on perceptual losses, and formalize the theory of consistency training [51, 52]. Stochastic consistency distillation introduces noise-aware consistency to better align with the teacher’s trajectories and improve sample quality at low NFE [53]. In parallel, rectified-flow training has been strengthened to compete with distillation in the low-step regime, showing that a single reflow iteration with improved timestep curricula and robust pre-metrics is often sufficient [54]. Flow-matching and flow trajectory distillation style approaches provide another route to few-step or one-step sampling by directly parameterizing ODE paths from noise to data [55, 56]. There is also growing interest in faster training of diffusion and consistency models themselves, which leverages cross-init consistency phenomena and curriculum-style schedules to cut training cost while retaining generation quality [57]. Together, these strategies reduce latency by one to two orders of magnitude, making diffusion practical for interactive applications and deployment under strict compute budgets.

### C. 3D Point Cloud Generation

This task is also referred to as shape generation. Achlioptas *et al.* [58] first proposed to study this problem, developing a straightforward GAN with multiple MLPs in both the generator and discriminator. They also introduced several metrics to evaluate the quality of 3D GANs. Valsesia *et al.* [59] improved the generator by incorporating graph convolution operations. Liu *et al.* [60] employed a tree-structured graph convolution network (GCN) to capture the hierarchical information of parent nodes. Gal *et al.* [61] used a GAN with multiple

roots to generate point sets that achieve unsupervised part disentanglement.

Beyond GAN-based methods, there are also approaches rooted in probability theory [62, 63, 64]. ShapeGF [65] used stochastic gradient ascent on an unnormalized probability density to move randomly sampled points toward high-density regions near the surface of a specific shape. DPM [1] conceptualized the transformation of points from a noise distribution to a point cloud as the inverse process of particle diffusion in a thermal system in contact with a heat bath. They modeled this inverse diffusion as a Markov chain conditioned on a particular shape. Yang *et al.* [2] introduced PointFlow, which generates point sets by modeling them as a distribution of distributions within a probabilistic framework. Kimura *et al.* [66] presented a flow-based model called ChartPointFlow, which constructs a map conditioned on a label, preserving the shape’s topological structure. Li *et al.* [67] developed a modified VAE for parts-aware editing and unsupervised point cloud generation.

Several methods have shown their effectiveness in the auto-encoding task using AE architectures, such as I-GAN [58], ShapeGF [65], and DPM [1]. However, despite advancements in point cloud generation, the implicit relationship between GANs and AEs, which offers significant prior information gain, remains largely unexplored.

## III. MULTI-SCALE LATENT POINT DIFFUSION MODELS AND LATENT CONSISTENCY MODELS

In this section, we will introduce our hierarchical VAE framework, the multi-scale latent point diffusion prior, and the latent consistency model.

### A. Hierarchical VAE Framework

We begin by formally introducing the latent diffusion framework, which is essentially a hierarchical VAE. We denote

a point cloud as  $X \in \mathbb{R}^{N \times 3}$ , consisting of  $N$  points with 3D coordinates. We then introduce a hierarchy of latent variables with different spatial scales/resolutions, denoting as  $\mathcal{Z} = \{Z^0, Z^1, \dots, Z^L\}$ , where  $L$  is the number of hierarchy levels. We use superscript to denote the index of scales. Here  $Z^l \in \mathbb{R}^{N_l \times C_l}$  where  $N_l$  and  $C_l$  are the number of points and the number of channels at the  $l$ -th level latent space respectively. Note that  $C_l = 3 + D_l$ , where  $D_l$  represents the extra dimension. At the 0-th, we have  $N_0 = N$  and  $N_l > N_{l+1}$  for any  $l = 0, \dots, L-1$ . In other words, the  $Z^0$  is latent point representation whereas  $Z^l$  are latent super-point (*i.e.*, a subset of points) representations for any  $l > 0$ . The details of latent layers and points in each level are demonstrated in Section IV.

The backbone of our hierarchical VAE consists of an encoder  $q_\phi(\mathcal{Z}|X)$ , a decoder  $p_\psi(X|\mathcal{Z})$ , and a prior  $p(\mathcal{Z})$ , where  $\phi$  and  $\psi$  are the learnable parameters. Specifically, our encoder is designed as follows,

$$q_\phi(\mathcal{Z}|X) := q_\phi(Z^L|X) \prod_{l=L-1}^0 q_\phi(Z^l|Z^{l+1}, X), \quad (1)$$

where  $q_\phi(Z^L|X)$  and  $q_\phi(Z^l|Z^{l+1}, X)$  are assumed to be factorized Gaussian distributions with learnable mean and fixed variance. Our decoder and prior take the simple form  $p_\psi(X|\mathcal{Z}) := p_\psi(X|Z^0)$  and  $p(\mathcal{Z}) := \prod_{l=0}^L p(Z^l)$  respectively. Here  $p(Z^l) := \mathcal{N}(\mathbf{0}, I)$ . The decoder  $p_\psi(X|\mathcal{Z})$  is parameterized as a factorized Laplace distribution with learnable means and unit scale, corresponding to an L1 reconstruction error.

The overall architecture is illustrated in Figure 1. As shown, both the encoder and the decoder consist of multiple Set Abstraction (SA) and Feature Propagation (FP) modules. Each SA module contains point-voxel convolution (PVC) layers [68], followed by a Grouper block, which includes the sampling and grouping layers introduced by [20]. Each FP module consists of a nearest-neighbor interpolation operation, followed by MLPs and PVC layers.

**First Stage Training.** We train the encoder and the decoder with a fixed prior by maximizing the modified evidence lower bound (ELBO),

$$\begin{aligned} \mathcal{L}_{\text{ELBO}}(\phi, \psi) = & \mathbb{E}_{p_{\text{data}}(X), q_\phi(\mathcal{Z}|X)} [\log p_\psi(X|\mathcal{Z}) \\ & - \lambda D_{KL}(q_\phi(\mathcal{Z}|X) \| p(\mathcal{Z}))]. \end{aligned} \quad (2)$$

Here  $p_{\text{data}}(X)$  represents the unknown data distribution of 3D point clouds. The hyperparameter  $\lambda$  controls the trade-off between the reconstruction error and the Kullback-Leibler (KL) divergence.

### B. Multi-Scale Latent Point Diffusion As Prior

After learning the encoder and the decoder in the first stage, we fix them and train a denoising diffusion based prior in the latent point space. Note that we have a set of latent representations  $\mathcal{Z} = \{Z^0, \dots, Z^L\}$  ranging from point to super-point levels output by the hierarchical encoder. It is natural to select the latent variable with the coarsest scale (lowest spatial resolution), *i.e.*,  $Z^L$ , to build a diffusion prior since it would enable efficient diffusion in a low-dimensional latent space.

However, as demonstrated in prior work [3], point-level latent variables remain crucial for producing high-quality 3D shapes. We thus focus on the point-level latent variable  $Z^0$  and design mechanisms to fuse multi-scale information. Specifically, we introduce a multi-scale latent point diffusion prior as below,

$$p(\mathcal{Z}) := p_\theta(Z^0|\mathcal{Z}^{\setminus 0}) \prod_{l=1}^L p_\theta(Z^l), \quad (3)$$

where  $\mathcal{Z}^{\setminus 0} = \{Z^1, \dots, Z^L\}$ . Here  $p_\theta(Z^l)$  is again a factorized standard Normal distribution, whereas  $p_\theta(Z^0|\mathcal{Z}^{\setminus 0})$  is a diffusion model. This design is crucial for enabling efficient sampling and consistency distillation, as it requires learning only one conditional prior while keeping others fixed. In contrast, previous work such as LION [3] needs to learn multiple priors corresponding to different levels in the hierarchy, which significantly complicates sampling and distillation. Similar to other diffusion models, our model consists of the forward and the reverse processes.

**Forward Process.** Following diffusion models [29], given initial latent point feature  $Z^0 \sim q_\phi(Z^0|X)$  output by the encoder, we gradually add noise as follows,

$$q(Z_{1:T}^0|Z^0, \mathcal{Z}^{\setminus 0}) := \prod_{t=1}^T q(Z_t^0|Z_{t-1}^0), \quad (4)$$

$$q(Z_t^0|Z_{t-1}^0) := \mathcal{N}(Z_t^0; \sqrt{1 - \beta_t} Z_{t-1}^0, \beta_t I), \quad (5)$$

where  $Z_0^0 := Z^0$  and we use subscripts to denote diffusion steps.  $T$  represents the number of diffusion steps,  $q(Z_t|Z_{t-1}^0)$  is a Gaussian transition probability with variance schedule  $\beta_1, \dots, \beta_T$ . We adopt a linear variance schedule in the diffusion process. The choice of  $\beta_t$  ensures that the chain approximately converges to the stationary distribution, *i.e.*, standard Gaussian distribution  $q(Z_T|Z^0, \mathcal{Z}^{\setminus 0}) \approx \mathcal{N}(Z_T; 0, I)$  after  $T$  steps.

**Reverse Process.** In the reverse process, given the initial noise  $Z_T^0 \sim \mathcal{N}(Z_T^0; \mathbf{0}, I)$ , we learn to gradually denoise to recover the observed latent point feature  $Z^0$  as follows,

$$p_\theta(Z_{0:T}^0|\mathcal{Z}^{\setminus 0}) := p(Z_T^0) \prod_{t=1}^T p_\theta(Z_{t-1}^0|Z_t^0, \mathcal{Z}^{\setminus 0}), \quad (6)$$

$$p_\theta(Z_{t-1}^0|Z_t^0, \mathcal{Z}^{\setminus 0}) := \mathcal{N}(Z_{t-1}^0; \mu_\theta(Z_t^0, t, \mathcal{Z}^{\setminus 0}), \sigma_t^2 I), \quad (7)$$

where the mean function  $\mu_\theta(\cdot, \cdot, \cdot)$  of the denoising distribution could be constructed by a neural network with learnable parameters  $\theta$ . In particular, following DDPM, we adopt the reparameterization  $\mu_\theta(Z_t^0, t, \mathcal{Z}^{\setminus 0}) = (Z_t^0 - \beta_t \epsilon_\theta(Z_t^0, t, \mathcal{Z}^{\setminus 0}) / \sqrt{1 - \bar{\alpha}_t}) / \sqrt{\alpha_t}$ , where  $\alpha_t := 1 - \beta_t$  and  $\bar{\alpha}_t := \prod_{s=1}^t \alpha_s$ . The variance  $\sigma_t$  is a hyperparameter and set to 1. Therefore, learning our multi-scale latent point diffusion prior is essentially learning the noise-prediction function  $\epsilon_\theta(\cdot, \cdot, \cdot)$  parameterized by  $\theta$ .

**Second Stage Training.** To train the prior, we ideally aim to minimize the KL divergence between the so-called *aggregated posterior*  $q(\mathcal{Z}) = \int p_{\text{data}}(X) q_\phi(\mathcal{Z}|X) dX$  and the prior  $p_\theta(\mathcal{Z})$ . However, it is again intractable so that we need to resort to the negative ELBO, which can be equivalently written as the

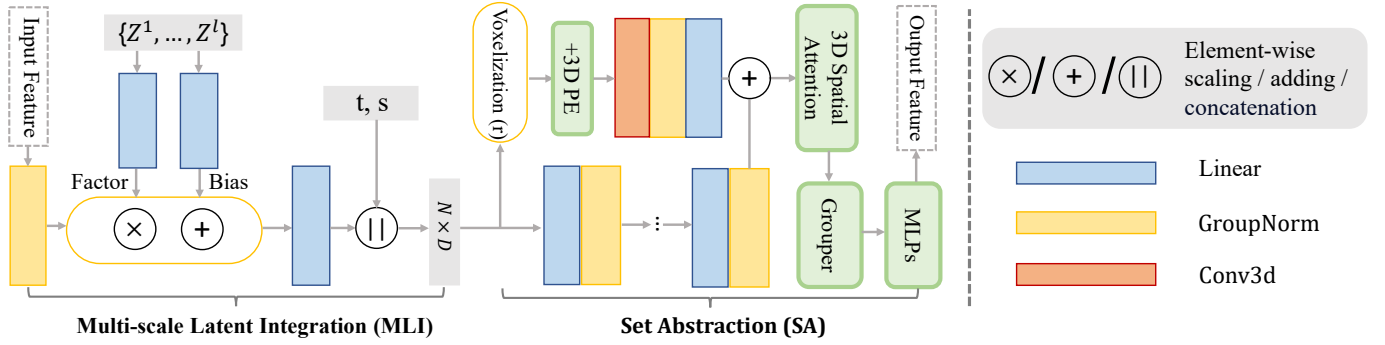


Fig. 2: An illustration of the network architecture of the latent diffusion prior. The multi-scale latent integration module injects higher-level latents to couple local geometry with global structure, while the set abstraction module downsamples and aggregates across scales. We denote the voxel grid size as  $r$ , and the hidden dimension as  $D$ .

following denoising score matching type of objective,

$$\mathcal{L}_{SM}(\theta) = \mathbb{E}_{t, X, \mathcal{Z}, \epsilon} \|\epsilon - \epsilon_{\theta}(Z_t^0, t, \mathcal{Z}^{\setminus 0})\|_2^2, \quad (8)$$

where the expectation is taken with respect to  $t \sim U([T])$ ,  $X \sim p_{\text{data}}(X)$ ,  $\mathcal{Z} \sim q_{\phi}(\mathcal{Z}|X)$ ,  $\epsilon \sim \mathcal{N}(\mathbf{0}, I)$ . Here  $U([T])$  is the uniform distribution over  $\{1, 2, \dots, T\}$ . Following [3], we utilize the mixed score parameterization, which linearly combines the input noisy sample and the noise predicted by the network, resulting in a residual correction that links the input and output of the noise function  $\epsilon_{\theta}$ . More details are provided in Supplementary Materials.

### C. Architecture Design

We now introduce the specific architecture of our noise prediction function  $\epsilon_{\theta}$ . Our backbone network is based on Point-Voxel CNNs (PVCNNs) [68]. To integrate multi-scale latent point feature, we propose the multi-scale latent integration (MLI) module before each SA and FP module of PVCNNs. We also adopt a 3D spatial attention mechanism in each point-voxel convolution (PVC) module, allowing the model to selectively attend to informative areas, as shown in Figure 2.

**Multi-Scale Latent Integration.** To better capture geometric patterns of 3D shapes, we propose the multi-scale latent integration (MLI) module to fuse latent variables across multiple scales/resolutions. As shown in Figure 2, at the diffusion step  $t$ , the  $s$ -th MLI module takes the feature map  $F_s$  as input, where  $F_0 = Z_t^0$ . Specifically, given the high-resolution feature map  $F_s$  and the target feature  $F$ , we modulate the normalized target feature  $F$  with the scaling parameters of both the two-dimensional scale and the high-scale features  $F^i$ , resulting in an intermediate representation as follows:

$$F_{s+1} = \left[ \text{MLP} \circ \text{ReLU}(\text{Linear}(\mathcal{Z}^{\setminus 0}) \odot \text{Norm}(F_s) + \text{Linear}(\mathcal{Z}^{\setminus 0})) \parallel \text{Pos}(t) \parallel \text{Pos}(k) \right], \quad (9)$$

where Norm is the layer normalization [69] and Linear denotes a linear layer. MLP consists of two linear layers.  $\odot$  denotes element-wise product and  $\circ$  means function composition.  $[\cdot \parallel \cdot]$  means concatenation of vectors. Pos( $\cdot$ ) is the positional embedding function. To enable scale-time awareness in the

model, we further modulate the feature with positional embedding of scale and time. The feature is fed to the following SA and FP modules to predict the noise.

**3D Spatial Attention Mechanism.** To help latent point representations better capture 3D spatial information, we design a 3D spatial attention mechanism. Our intuition is that closer points in 3D space would have a stronger correlation, thus higher attention values. We introduce a pairwise bias term that depends on the 3D distances between points. Specifically, in PVC, following [68], we first use PointNet++ [20] to extract the local features  $F_p$  from the point cloud. We then convert the point cloud data into voxels, enabling the application of 3D convolution operations to obtain voxel features  $F_v$ . These are then fused to get the combined feature  $F_a = \text{Add}(F_p, \text{MLP}(F_v))$ . For  $F_a$ , we compute the pairwise spatial distance matrix  $B \in \mathbb{R}^{n^i \times n^i}$  between different point pairs at the current scale, where  $n^i$  is the number of points at the current scale  $i$ , and use it as a bias in computing the attention,

$$F_a = \text{softmax} \left( \frac{QK^T}{\sqrt{d}} + B \right) \cdot V, \quad (10)$$

where  $Q$ ,  $K$ , and  $V$  are query, key, and value respectively in the standard attention module. We add this module to each PVC layer across all scales to make the model’s attention conform to the 3D distances between points. Additionally, following [17], we add 3D positional embeddings to adaptively aggregate feature from voxelized point clouds. In each PVC layer, given voxelized input  $V \in \mathbb{R}^{v \times v \times v \times c}$ , where  $c$  is the embedding dimension and  $v^3$  denotes the number of voxelized tokens, we add sine-cosine-based 3D positional embeddings to all input tokens.

### D. Multi-Scale Latent Point Consistency Models

Since the diffusion models are notoriously slow in sampling, we explore the consistency models (CMs) [33] in the latent diffusion framework to accelerate the generation of 3D shapes. At the core of CMs, a consistency map is introduced to map any noisy data point on the trajectory of probability-flow ordinary differential equations (PF-ODEs) to the starting point, *i.e.*, clean data. There are two ways to train such a consistency map [33], *i.e.*, consistency distillation and consistency training.

The former requires a pretrained teacher model whereas the latter trains the consistency map from scratch. We explored both options and found consistency distillation works well, whereas consistency training is sensitive to hyperparameters.

Specifically, we first rewrite the reverse process in the continuous-time setting following [32, 36],

$$\frac{dZ_t^0}{dt} = \frac{d \log \alpha_t}{dt} Z_t^0 + \left( \frac{d \log \alpha_t}{2\sigma_t dt} - \frac{d \log \alpha_t}{dt} \sigma_t \right) \epsilon_\theta(Z_t^0, t, \mathcal{Z}^{\setminus 0}), \quad (11)$$

where  $\epsilon_\theta(Z_t^0, t, \mathcal{Z}^{\setminus 0})$  is the noise prediction model and  $\alpha_t, \sigma_t$  are determined by the noise schedule as aforementioned. Samples can be drawn by solving the PF-ODE from  $T$  to 0. To achieve consistency distillation, we introduce a consistency map  $f_{\hat{\theta}} : (Z_t^0, t, \mathcal{Z}^{\setminus 0}) \mapsto Z_0^0$  to directly predict the solution of PF-ODE in Equation 11. For  $t = 0$ , we parameterize  $f_{\hat{\theta}}$  using the noise prediction model  $\hat{\epsilon}_\theta$ :

$$f_{\hat{\theta}}(Z_t^0, t, \mathcal{Z}^{\setminus 0}) = c_{\text{skip}}(t)Z_t^0 + c_{\text{out}}(t) \left( \frac{Z_t^0 - \sigma_t \hat{\epsilon}_{\hat{\theta}}(Z_t^0, t, \mathcal{Z}^{\setminus 0})}{\alpha_t} \right), \quad (12)$$

where  $c_{\text{skip}}(0) = 1$ ,  $c_{\text{out}}(0) = 0$ , and  $\hat{\epsilon}_{\hat{\theta}}(z, c, t)$  is a noise prediction model whose initialized parameters are the same as those of the teacher diffusion model. Note that  $f_{\hat{\theta}}$  can be parameterized in various ways, depending on the teacher model’s parameterization of the diffusion model.

We assume that an effective ODE solver can be used to approximate the integral on the right side of Equation 11 from any starting time to the ending time. Note that we only use the solver during training and not during sampling. We aim to predict the solution of the PF-ODE by minimizing the consistency distillation loss [33]:

$$\mathcal{L}_{\text{CD}}(\hat{\theta}, \hat{\theta}^-; \Psi) = \mathbb{E}_{n, \mathcal{Z}^{\setminus 0}, Z_{t_{n+1}}^0} \left[ d \left( f_{\hat{\theta}} \left( Z_{t_{n+1}}^0, \mathcal{Z}^{\setminus 0}, t_{n+1} \right), f_{\hat{\theta}^-} \left( \hat{Z}_{t_n}^0, \mathcal{Z}^{\setminus 0}, t_n \right) \right) \right], \quad (13)$$

where  $\hat{Z}_{t_n}^0 = Z_{t_{n+1}}^0 + (t_n - t_{n+1})\Psi(Z_{t_{n+1}}^0, t_{n+1}, t_n, \mathcal{Z}^{\setminus 0})$  is the solution of the PF-ODE obtained via calling the ODE solver  $\Psi$  from time  $t_{n+1}$  to  $t_n$ . Here  $d(\mathbf{x}, \mathbf{y}) = \|\mathbf{x} - \mathbf{y}\|_2^2$  denotes the discrepancy between two latent points, which penalizes large deviations more heavily and thus provides a smooth, scale-aware objective in the latent space.

#### IV. EXPERIMENTS

In this section, we train the multi-scale latent diffusion model on the Shapenet dataset and obtain MLPCM using the latent consistent distillation. We first introduce the dataset and evaluation metrics. Then we evaluate the performance of MLPCM on the Single-class 3D point cloud generation task. Next, we compare the results of MLPCM with a large number of baselines on multi-class unconditional 3D shape generation in terms of the performance, sampling time, and model parameters. Finally, we give a detailed ablation study on the effectiveness of individual contributions.

#### A. Datasets

For the unconditional 3D point cloud generation task, we utilize the ShapeNet dataset [70] as pre-processed and provided by PointFlow [2], ensuring consistency with prior studies. To facilitate fair comparisons with existing baseline methods [1, 2, 3, 17, 71], we focus on three commonly used categories: airplane, chair, and car. Each shape in the dataset contains 15,000 points, and during training, we randomly sample 2,048 points per shape in each iteration. The training dataset includes 2,832 shapes for airplanes, 4,612 for chairs, and 2,458 for cars.

We evaluate sample quality using a standard reference set, which consists of 405, 662, and 352 shapes for airplanes, chairs, and cars, respectively. Consistent with the normalization approach in PointFlow [2] and LION [3], the data is normalized globally across all shapes. Specifically, we calculate the mean values for each axis and a single standard deviation across all axes based on the entire training set. This ensures that the input data is standardized for training and comparison purposes.

While reproducing baseline methods on the ShapeNet dataset provided by PointFlow [2], we observed that certain approaches [3, 65, 72, 73, 74] utilize per-shape normalization. This involves calculating the mean for each axis individually for each shape and determining the scale based on the maximum extent across all axes for that shape. Consequently, the point coordinates are constrained within the range of [-1, 1]. For comparisons with these methods, we adhere to the same normalization strategy during both training and evaluation of our model. It is worth noting that these varying normalization schemes lead to fundamentally different generative modeling tasks. Therefore, ensuring clarity about these setups is crucial for fair and meaningful comparisons.

#### B. Implementation Details

**Training Details** Our teacher model is implemented in PyTorch [75]. The VAE is trained for around 8000 epochs with an initial learning rate of 0.001, and we use Adam [76] to optimize the entire model. The batch size is set to 128, the latent point dimension is 4, and the skip weight is set to 0.01. The diffusion prior is trained for approximately 24,000 epochs with an initial learning rate of 0.0002, using 1000 time steps for the diffusion process, with a linear schedule for  $\beta_t$ . We train MLPCM for 100K iterations with a batch size of 128, a learning rate of  $2 \times 10^{-4}$ , and an EMA rate  $\mu = 0.99995$ . Both the VAE and the diffusion prior are trained on 8 NVIDIA A40 GPUs.

For the mixed denoising score network parametrization used in our teacher model, we follow the approach of [77]. Specifically, the denoising model is parameterized as an analytically optimal denoising network for a normal data distribution, augmented with a neural network-based correction. This design is particularly advantageous when the modeled distribution is close to normal, as is the case here. In the first training stage, all latent encodings are regularized to approximate a standard normal distribution due to the Kullback-Leibler regularization in the VAE objective. Our implementation of the

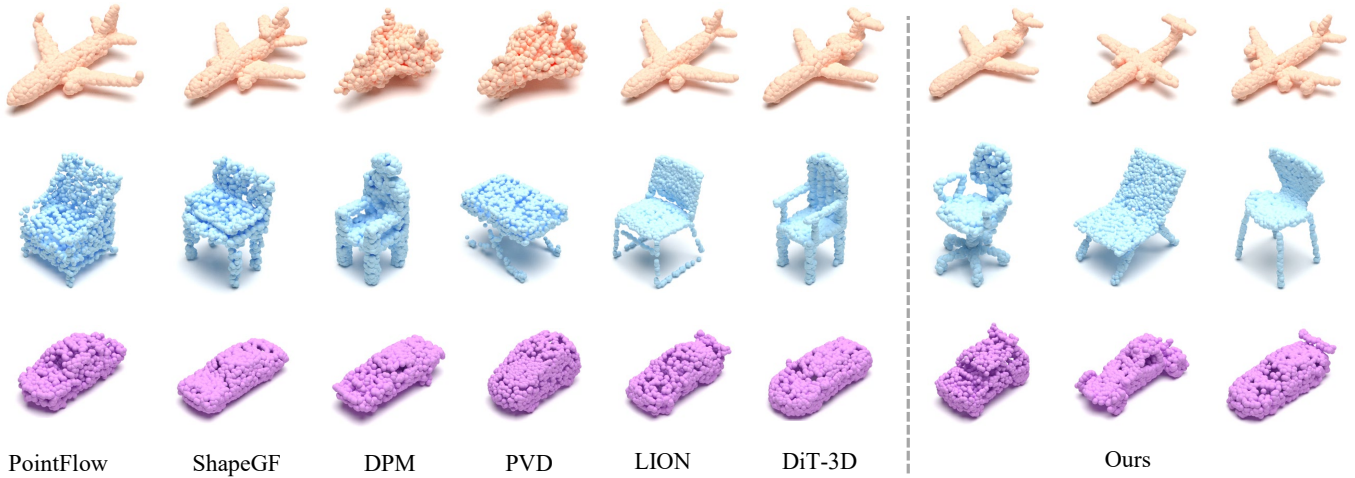


Fig. 3: Unconditional shape generation with 2,048 points for the classes *airplane*, *car*, and *chair* using class-specific models, trained on the ShapeNet dataset from PointFlow with global normalization. Our samples better represent component relationships, such as the seat-leg connection and the wing-fuselage connection, while competing approaches exhibit smaller gaps, fused components, or asymmetries between mirrored components.

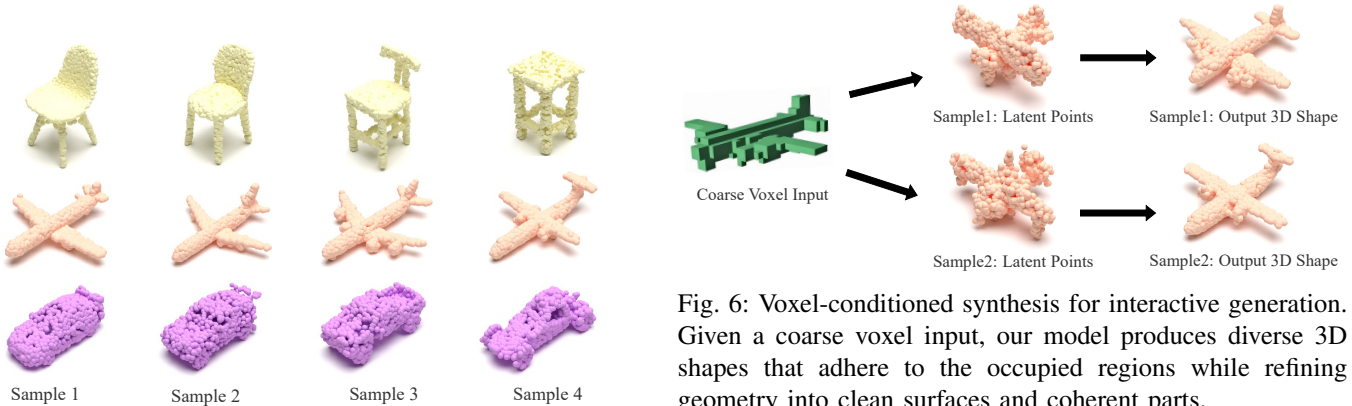


Fig. 4: Qualitative visualizations of high-fidelity and diverse 3D point cloud generation. Generated shapes preserve physically plausible structure and global topology while varying fine details, demonstrating diversity without sacrificing symmetry.

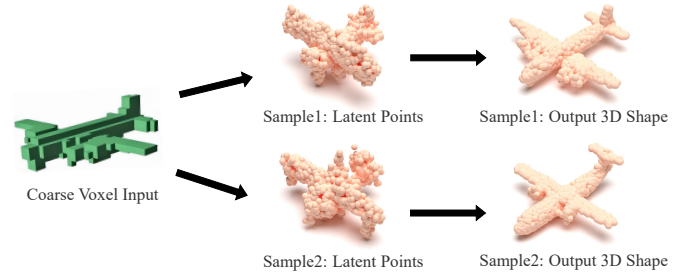


Fig. 6: Voxel-conditioned synthesis for interactive generation. Given a coarse voxel input, our model produces diverse 3D shapes that adhere to the occupied regions while refining geometry into clean surfaces and coherent parts.

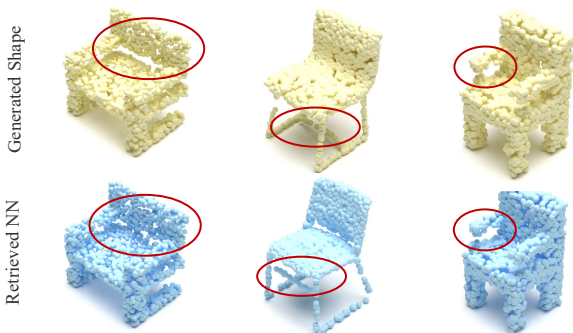


Fig. 5: Comparison between generated shapes and retrieved nearest neighbors (NN) in the training dataset. The generated shapes closely match the ground-truth shapes in overall topology, yet differ in fine-grained details, demonstrating diversity.

mixed denoising score network strictly adheres to the method described by [77], and we direct readers to their work for additional details.

For the latent consistency model, to align with the discrete-time schedule in our multi-scale latent diffusion model, which synthesizes shapes over 1000 DDPM steps, we employ DDIM [31] as the PF-ODE solver.

**Evaluation Metrics** Following recent works [2, 3, 71], we use 1-NNA, with both Chamfer distance (CD) and earth mover distance (EMD), as our main metric. It quantifies the similarity between the distribution of generated shapes and that of shapes from the validation set and measures both quality and diversity [2].

### C. Single-Class 3D Point Cloud Generation

**Implementation** Our implementation is based on the PyTorch. The input point cloud size is  $2048 \times 3$ . Both our VAE encoder and decoder are built upon PVCNN [68], consisting of 4 layers of SA modules and FP modules. The voxel grid sizes of PVC at different scales are 32, 16, 8, and 8, respectively. We adopt the Farthest Point Sampling (FPS) algorithm for

sampling in the Grouper block, with the sampled center points being 1024, 256, 64, and 16. KNN (K-Nearest Neighbors) is used to aggregate local neighborhood features, with 32 neighbors for each point in the Grouper. We apply a dropout rate of 0.1 to all dropout layers in the VAE. Following [3], we initialize our VAE model so that it acts as an identity mapping between the input, latent space, and reconstruction points at the start of training. We achieve this by reducing the variance of the encoder and correspondingly weighting the skip connections. Our latent prior also consists of 4 layers of SA modules and FP modules. The time embedding and multi-scale latent representations are concatenated with the point features at the input of each corresponding SA and FP layer. We adopt the hybrid denoising score network parameterization following [3].

**Results** We validate our model’s results under two settings: normalizing data across the entire dataset and normalizing each shape individually. Samples from MLPCM are shown in Figure 3 and Figure 4, and quantitative results are provided in Table I and Table II. For airplanes, our results better preserve thin structures and global symmetry, with crisper wing contours and fewer broken tips. Competing methods often exhibit wing thickening, tail erosion, or rough leading edges, especially in PointFlow and ShapeGF, while DiT-3D improves the silhouette but still shows uneven point density around the tail. For chairs, our method maintains slender legs with consistent spacing and recovers backrest curvature and armrest topology with clear connectivity, while other methods produce floating clusters near the seat or excessively smoothed armrests. Although LION and PVD capture the overall shape, they lose fine perforations and edge sharpness. For cars, our generations show clearly defined wheel arch depressions and fewer surface pits, whereas other methods yield blotchy bodies with collapsed cavities or roof perforations. DPM and ShapeGF in particular display pronounced surface granularity and local self-intersections.

More visual results generated by our multi-scale latent consistency model are demonstrated in Figure 7. Overall, our model achieves sharper thin structures, cleaner topology, and more uniform point distributions, leading to higher structural fidelity than other methods.

Note that TM stands for Teacher Model and LCM stands for Latent Consistency Models. MLPCM outperforms all baselines and achieves state-of-the-art performance across all categories and dataset versions. Compared to key baselines like DPM, PVD, and LION, our samples are diverse and have a better visual quality.

#### D. Multi-Class 3D Shape Generation

Following [3], we also jointly trained the multi-scale latent diffusion model and the MLPCM model across 13 different categories (airplane, chair, car, lamp, table, sofa, cabinet, bench, phone, watercraft, speaker, display, ship, rifle). Due to the highly complex and multi-modal data distribution, jointly training a model is challenging.

We validated the model’s generation performance on the Shapenet-Vol dataset, where each shape is normalized, meaning the point coordinates are bounded within  $[-1, 1]$ . We report

the quantitative results in Table III, comparing our method with various strong baselines under the same setting. We found that the proposed multi-scale latent diffusion model significantly outperforms all baselines, and MLPCM greatly improves sampling efficiency while maintaining performance.

#### E. Comparison with Nearest Neighbors and Voxel-guided Shape Synthesis

It is widely acknowledged that 1-NNA serves as the primary evaluation metric in this field, largely because no superior alternative currently exists. However, it can be misleading, as perfect memorization of the training set would yield an excellent score. Therefore, we adopt a more informative analysis that present the generated shape alongside its retrieved nearest neighbor, highlighting their structural and semantic similarity while also illustrating diversity in finer details. Specifically, Fig. 5 compares our generated shapes (top) with their retrieved Chamfer-nearest neighbors (bottom). Global topology aligns closely, while fine details differ, confirming the diversity.

To supplement the conditional generation experiment to observe the generalization diversity of the model, We add voxel guided generation results as shown in Fig. 6. We begin by voxelizing the training set and fine-tuning our encoder networks to learn representations that can be accurately decoded back into the original shapes. For voxelized inputs processed with our point-cloud networks, we further sample surface points from the voxels to serve as input data.

#### F. Sampling Time

The proposed multi-scale latent diffusion model synthesizes shapes using 1000 steps of DDPM, while MLPCM synthesizes them using only 1-4 steps, generating high-quality shapes in under 0.5 seconds. This makes real-time interactive applications feasible. In Table IV, we compare the sampling time and quality of generating a point cloud sample (2048 points) from noise using different DDPM, DDIM [31] sampling methods, and MLPCM. When using  $\leq 10$  steps, DDIM’s performance degrades significantly, whereas MLPCM can produce visually high-quality shapes in just a few steps or even one step.

#### G. Ablation Study

In this section, we conduct the ablation study to investigate the effectiveness of the individual design components introduced in the multi-scale latent diffusion model, including the multi-scale latents, 3D Spatial Attention Mechanism, and the additional dimensions of the latent points.

**Ablation on the Key Design Components.** We perform the ablation study on the Car category. For the configuration without multi-scale latent representations, we consider two scenarios: one using only point-level latent features to capture fine-grained details and another using only shape-level features to focus on global structure. This allows us to assess the impact of each representation scale individually. The model sizes are kept nearly identical across all settings to ensure fair comparison. As shown in Table V, the full model, integrating multi-scale latent representations and the 3D spatial



Fig. 7: More visualization of Unconditional 3D shape generation via the proposed multi-scale latent consistency model on the airplane, car, and chair categories.

TABLE I: Generation metrics (1-NNA $\downarrow$ ) on airplane, chair, car categories from ShapeNet dataset from PointFlow [2]. Training and test data normalized globally into [-1, 1]. TM stands for Teacher Model and LCM stands for Latent Consistency Models.

Method	Airplane		Chair		Car	
	CD	EMD	CD	EMD	CD	EMD
r-GAN [58]	98.40	96.79	83.69	99.70	94.46	99.01
l-GAN (CD) [58]	87.30	93.95	68.58	83.84	66.49	88.78
l-GAN (EMD) [58]	89.49	76.91	71.90	64.65	71.16	66.19
PointFlow [2]	75.68	70.74	62.84	60.57	58.10	56.25
SoftFlow [15]	76.05	65.80	59.21	60.05	64.77	60.09
SetVAE [78]	76.54	67.65	58.84	60.57	59.94	59.94
DPF-Net [16]	75.18	65.55	62.00	58.53	62.35	54.48
DPM [1]	76.42	86.91	60.05	74.77	68.89	79.97
PVD [71]	73.82	64.81	56.26	53.32	54.55	53.83
LION [3]	67.41	61.23	53.70	52.34	53.41	51.14
MeshDiffusion [79]	66.44	76.26	53.69	57.63	81.43	87.84
DiT-3D [17]	69.42	65.08	55.59	54.91	53.87	53.02
Ours (TM)	<b>65.12</b>	<b>58.70</b>	<b>51.48</b>	<b>50.06</b>	<b>51.17</b>	<b>48.92</b>
Ours (LCM)	67.22	60.32	53.63	51.74	53.82	52.75

TABLE II: Generation results (1-NNA $\downarrow$ ) on ShapeNet dataset from PointFlow [2]. All data normalized individually into [-1, 1].

Method	Airplane		Chair		Car	
	CD	EMD	CD	EMD	CD	EMD
Tree-GAN [60]	97.53	99.88	88.37	96.37	89.77	94.89
ShapeGF [65]	81.23	80.86	58.01	61.25	61.79	57.24
SP-GAN [72]	94.69	93.95	72.58	83.69	87.36	85.94
PDGN [74]	94.94	91.73	71.83	79.00	89.35	87.22
GCA [73]	88.15	85.93	64.27	64.50	70.45	64.20
LION [3]	76.30	67.04	56.50	53.85	59.52	49.29
Ours (TM)	<b>73.28</b>	<b>63.08</b>	<b>56.20</b>	<b>53.16</b>	<b>58.31</b>	<b>47.74</b>
Ours (LCM)	75.56	66.85	58.58	55.32	61.28	49.91

TABLE III: Results of joint train on 13 classes of ShapeNet-vol.

Method	CD (1- NNA $\downarrow$ )	EMD (1- NNA $\downarrow$ )
Tree-GAN [60]	96.80	96.60
PointFlow [2]	63.25	66.05
ShapeGF [65]	55.65	59.00
SetVAE [78]	79.25	95.25
PDGN [74]	71.05	86.00
DPF-Net [16]	67.10	64.75
DPM [1]	62.30	86.50
PVD [71]	58.65	57.85
LION [3]	51.85	48.95
Ours (TM)	<b>50.17</b>	<b>47.84</b>
Ours (LCM)	53.85	52.45

attention mechanism, consistently outperforms the simplified settings across all evaluation metrics. This demonstrates the effectiveness of combining fine-grained local information with global shape context, along with the attention mechanism, in achieving more accurate and coherent reconstructions.

**Ablation on Extra Dimension for Latent Points.** We ablate the additional latent point dimension  $D_l$  on the Car category in Table VI. We experimented with several different additional dimensions for the latent points, ranging from 0 to 5, where  $D_l = 1$  provided the best overall performance. As the additional dimensions increase, we observe a decrease in the 1-NNA score. We thus use  $D_l = 1$  for all other experiments.

**Ablation on different backbones.** We conduct an ablation study to evaluate different neural network architectures for processing point clouds in the encoder, decoder, and diffusion prior. The results, presented in Table VII, focus on the car category using the teacher model, consistent with other ablation studies. We test four popular backbone architectures: Point-Voxel CNN (PVCNN) [68], Dynamic Graph CNN (DGCNN) [21], PointTransformer [80], and PointTransformerV2 [81]. Among these, PVCNN demonstrates the best overall performance, making it our architecture of choice.

**Ablation on 3D Positional Encoding.** We conduct an ablation study to evaluate different 3D positional encoding methods. In the Voxel Positional Encoding (VPE) approach, we applied frequency-based sine-cosine 3D positional embeddings to the point-voxel branch in the SA module, following the design of DiT-3D [17]. For Contextual Relative Positional Encoding (cRPE), inspired by the Stratified Transformer [82], we enhanced the traditional positional encoding in the attention mechanism by adding a vector representing the positional offset between Query and Key during each attention computation. The experiments were performed on the car category, with results summarized in Table VIII. The findings show that omitting 3D positional encoding leads to significantly poorer

TABLE IV: The sampling rates and generation quality of our model with various methods. Our approach achieves high-quality shape generation within 0.5 seconds while maintaining quality.

Method	steps	time (sec)	CD (1- NNA↓)	EMD (1- NNA↓)
LION (DDPM) [3]	1000	27.09	53.41	51.14
LION (DDIM) [3]	1000	27.09	54.85	53.26
LION (DDIM) [3]	100	3.07	56.04	54.97
LION (DDIM) [3]	10	0.47	90.38	95.4
Ours (TM)	1000	25.16	<b>51.17</b>	<b>48.92</b>
Ours (LCM)	1	<b>0.18</b>	79.46	82.00
Ours (LCM)	4	0.31	53.82	52.75

TABLE V: Ablation studies on key 3D design components on the car category. PL and SL represent the point-level latents and shape-level latents, respectively, and 3DSA represents the 3D Spatial Attention Mechanism.

PL	SL	3DSA	CD (1- NNA↓)	EMD (1- NNA↓)
	✓	✓	74.29	72.81
✓		✓	53.40	51.96
✓	✓		53.02	50.75
✓	✓	✓	<b>51.17</b>	<b>48.92</b>

TABLE VI: Ablation on the number of extra dimension  $D_l$  of the latent points, on the car category.

Extra Latent Dim	CD (1- NNA↓)	EMD (1- NNA↓)
0	54.56	52.79
1	<b>51.17</b>	<b>48.92</b>
3	56.88	55.27
5	59.06	51.90

TABLE VII: Ablation study on the backbone of the encoder and decoder of hierarchical VAE and diffusion prior on the car category for Teacher Model. For DGCNN, we try different numbers of top-k nearest neighbors(knn).

Backbone	CD (1- NNA↓)	EMD (1- NNA↓)
DGCNN (knn=10)	67.66	57.08
DGCNN (knn=20)	68.54	57.60
PointTransformer	89.41	86.52
PointTransformerV2	80.09	79.57
PVCNN	<b>51.17</b>	<b>48.92</b>

TABLE VIII: Ablation study on 3D positional encoding on the car category for Teacher Model.

Settings	CD (1- NNA↓)	EMD (1- NNA↓)
w/o 3D PE	51.60	49.38
with VPE	51.17	<b>48.92</b>
with cRPE	<b>51.10</b>	49.08

generation results. While VPE and cRPE achieve comparable outcomes, we selected VPE as our 3D positional encoding method for its simplicity and effectiveness.

## V. CONCLUSION

In this paper, we propose the Multi-Scale Latent Point Consistency Model (MLPCM) to address the task of efficient point-cloud-based 3D shape generation. We first construct a multi-scale latent diffusion model, which includes a point encoder based on multi-scale voxel convolutions, a multi-scale denoising diffusion prior with 3D spatial attention, and a voxel-convolution-based decoder. The diffusion prior model, which integrates multi-scale information, effectively captures both local and global geometric features of 3D objects, while the 3D spatial attention mechanism helps the model better capture spatial information and feature correlations. Moreover, MLPCM leverages consistency distillation to compress the prior into a one-step generator. On the widely used ShapeNet and ShapeNet-Vol datasets, the proposed multi-scale latent diffusion model achieves state-of-the-art performance, and MLPCM achieves a 100x speedup during sampling while surpassing the state-of-the-art diffusion models in terms of shape quality and diversity. In the future, we are interested in extending MLPCM to other diverse 3D representations such as meshes.

## REFERENCES

- [1] S. Luo and W. Hu, "Diffusion probabilistic models for 3d point cloud generation," in *Proceedings of the IEEE/CVF conference on computer vision and pattern recognition*, 2021, pp. 2837–2845.
- [2] G. Yang, X. Huang, Z. Hao, M.-Y. Liu, S. Belongie, and B. Hariharan, "Pointflow: 3d point cloud generation with continuous normalizing flows," in *Proceedings of the IEEE/CVF international conference on computer vision*, 2019, pp. 4541–4550.
- [3] X. Zeng, A. Vahdat, F. Williams, Z. Gojcic, O. Litany, S. Fidler, K. Kreis *et al.*, "Lion: Latent point diffusion models for 3d shape generation," *Advances in Neural Information Processing Systems*, vol. 35, pp. 10021–10039, 2022.
- [4] B. Du, X. Gao, W. Hu, and R. Liao, "Generative 3d part assembly via part-whole-hierarchy message passing," in *Proceedings of the IEEE/CVF Conference on Computer Vision and Pattern Recognition*, 2024, pp. 20 850–20 859.
- [5] M. Liu, R. Shi, L. Chen, Z. Zhang, C. Xu, X. Wei, H. Chen, C. Zeng, J. Gu, and H. Su, "One-2-3-45++: Fast single image to 3d objects with consistent multi-view generation and 3d

- diffusion,” in *Proceedings of the IEEE/CVF conference on computer vision and pattern recognition*, 2024, pp. 10072–10083.
- [6] Y. Siddiqui, T. Monnier, F. Kokkinos, M. Kariya, Y. Kleiman, E. Garreau, O. Gafni, N. Neverova, A. Vedaldi, R. Shapovalov *et al.*, “Meta 3d assetgen: Text-to-mesh generation with high-quality geometry, texture, and pbr materials,” *Advances in Neural Information Processing Systems*, vol. 37, pp. 9532–9564, 2024.
- [7] S. Wu, Y. Lin, F. Zhang, Y. Zeng, J. Xu, P. Torr, X. Cao, and Y. Yao, “Direct3d: Scalable image-to-3d generation via 3d latent diffusion transformer,” *Advances in Neural Information Processing Systems*, vol. 37, pp. 121 859–121 881, 2024.
- [8] O. Litany, A. Bronstein, M. Bronstein, and A. Makadia, “Deformable shape completion with graph convolutional autoencoders,” in *Proceedings of the IEEE conference on computer vision and pattern recognition*, 2018, pp. 1886–1895.
- [9] Q. Tan, L. Gao, Y.-K. Lai, and S. Xia, “Variational autoencoders for deforming 3d mesh models,” in *Proceedings of the IEEE conference on computer vision and pattern recognition*, 2018, pp. 5841–5850.
- [10] P. Mittal, Y.-C. Cheng, M. Singh, and S. Tulsiani, “Autosdf: Shape priors for 3d completion, reconstruction and generation,” in *Proceedings of the IEEE/CVF Conference on Computer Vision and Pattern Recognition*, 2022, pp. 306–315.
- [11] J. Wu, C. Zhang, T. Xue, B. Freeman, and J. Tenenbaum, “Learning a probabilistic latent space of object shapes via 3d generative-adversarial modeling,” *Advances in neural information processing systems*, vol. 29, 2016.
- [12] D. W. Shu, S. W. Park, and J. Kwon, “3d point cloud generative adversarial network based on tree structured graph convolutions,” in *Proceedings of the IEEE/CVF international conference on computer vision*, 2019, pp. 3859–3868.
- [13] Z. Hao, A. Mallya, S. Belongie, and M.-Y. Liu, “Gancraft: Unsupervised 3d neural rendering of minecraft worlds,” in *Proceedings of the IEEE/CVF International Conference on Computer Vision*, 2021, pp. 14 072–14 082.
- [14] T. Karras, S. Laine, and T. Aila, “A style-based generator architecture for generative adversarial networks,” in *Proceedings of the IEEE/CVF conference on computer vision and pattern recognition*, 2019, pp. 4401–4410.
- [15] H. Kim, H. Lee, W. H. Kang, J. Y. Lee, and N. S. Kim, “Softflow: Probabilistic framework for normalizing flow on manifolds,” *Advances in Neural Information Processing Systems*, vol. 33, pp. 16 388–16 397, 2020.
- [16] R. Klokov, E. Boyer, and J. Verbeek, “Discrete point flow networks for efficient point cloud generation,” in *European Conference on Computer Vision*. Springer, 2020, pp. 694–710.
- [17] S. Mo, E. Xie, R. Chu, L. Hong, M. Niessner, and Z. Li, “Dit-3d: Exploring plain diffusion transformers for 3d shape generation,” *Advances in neural information processing systems*, vol. 36, pp. 67 960–67 971, 2023.
- [18] X. Ren, J. Huang, X. Zeng, K. Museth, S. Fidler, and F. Williams, “Xcube: Large-scale 3d generative modeling using sparse voxel hierarchies,” in *Proceedings of the IEEE/CVF Conference on Computer Vision and Pattern Recognition*, 2024, pp. 4209–4219.
- [19] C. R. Qi, H. Su, K. Mo, and L. J. Guibas, “Pointnet: Deep learning on point sets for 3d classification and segmentation,” in *Proceedings of the IEEE conference on computer vision and pattern recognition*, 2017, pp. 652–660.
- [20] C. R. Qi, L. Yi, H. Su, and L. J. Guibas, “Pointnet++: Deep hierarchical feature learning on point sets in a metric space,” *Advances in neural information processing systems*, vol. 30, 2017.
- [21] Y. Wang, Y. Sun, Z. Liu, S. E. Sarma, M. M. Bronstein, and J. M. Solomon, “Dynamic graph cnn for learning on point clouds,” *ACM Transactions on Graphics (tog)*, vol. 38, no. 5, pp. 1–12, 2019.
- [22] W. Yuan, T. Khot, D. Held, C. Mertz, and M. Hebert, “Pcn: Point completion network,” in *2018 international conference on 3d vision (3DV)*. IEEE, 2018, pp. 728–737.
- [23] L. P. Tchapmi, V. Kosaraju, H. Rezatofighi, I. Reid, and S. Savarese, “Topnet: Structural point cloud decoder,” in *Proceedings of the IEEE/CVF conference on computer vision and pattern recognition*, 2019, pp. 383–392.
- [24] F. Fuchs, D. Worrall, V. Fischer, and M. Welling, “Se (3)-transformers: 3d roto-translation equivariant attention networks,” *Advances in neural information processing systems*, vol. 33, pp. 1970–1981, 2020.
- [25] V. G. Satorras, E. Hoogeboom, and M. Welling, “E (n) equivariant graph neural networks,” in *International conference on machine learning*. PMLR, 2021, pp. 9323–9332.
- [26] R. Rombach, A. Blattmann, D. Lorenz, P. Esser, and B. Ommer, “High-resolution image synthesis with latent diffusion models,” in *Proceedings of the IEEE/CVF conference on computer vision and pattern recognition*, 2022, pp. 10 684–10 695.
- [27] A. Vahdat and J. Kautz, “Nvae: A deep hierarchical variational autoencoder,” *Advances in neural information processing systems*, vol. 33, pp. 19 667–19 679, 2020.
- [28] R. Child, “Very deep vaes generalize autoregressive models and can outperform them on images,” *arXiv preprint arXiv:2011.10650*, 2020.
- [29] J. Ho, A. Jain, and P. Abbeel, “Denoising diffusion probabilistic models,” *Advances in neural information processing systems*, vol. 33, pp. 6840–6851, 2020.
- [30] J. Ho and T. Salimans, “Classifier-free diffusion guidance,” *arXiv preprint arXiv:2207.12598*, 2022.
- [31] J. Song, C. Meng, and S. Ermon, “Denoising diffusion implicit models,” *arXiv preprint arXiv:2010.02502*, 2020.
- [32] C. Lu, Y. Zhou, F. Bao, J. Chen, C. Li, and J. Zhu, “Dpm-solver: A fast ode solver for diffusion probabilistic model sampling in around 10 steps,” *Advances in Neural Information Processing Systems*, vol. 35, pp. 5775–5787, 2022.
- [33] Y. Song, P. Dhariwal, M. Chen, and I. Sutskever, “Consistency models,” *arXiv preprint arXiv:2303.01469*, 2023.
- [34] C. Lu, Y. Zhou, F. Bao, J. Chen, C. Li, and J. Zhu, “Dpm-solver++: Fast solver for guided sampling of diffusion probabilistic models,” *arXiv preprint arXiv:2211.01095*, 2022.
- [35] Y. Song and S. Ermon, “Generative modeling by estimating gradients of the data distribution,” *Advances in neural information processing systems*, vol. 32, 2019.
- [36] Y. Song, J. Sohl-Dickstein, D. P. Kingma, A. Kumar, S. Ermon, and B. Poole, “Score-based generative modeling through stochastic differential equations,” *arXiv preprint arXiv:2011.13456*, 2020.
- [37] Y. Song, C. Durkan, I. Murray, and S. Ermon, “Maximum likelihood training of score-based diffusion models,” *Advances in neural information processing systems*, vol. 34, pp. 1415–1428, 2021.
- [38] A. Ramesh, P. Dhariwal, A. Nichol, C. Chu, and M. Chen, “Hierarchical text-conditional image generation with clip latents,” *arXiv preprint arXiv:2204.06125*, vol. 1, no. 2, p. 3, 2022.
- [39] A. Nichol, P. Dhariwal, A. Ramesh, P. Shyam, P. Mishkin, B. McGrew, I. Sutskever, and M. Chen, “Glide: Towards photorealistic image generation and editing with text-guided diffusion models,” *arXiv preprint arXiv:2112.10741*, 2021.
- [40] D. P. Kingma, “Auto-encoding variational bayes,” *arXiv preprint arXiv:1312.6114*, 2013.
- [41] K. Sohn, H. Lee, and X. Yan, “Learning structured output representation using deep conditional generative models,” *Advances in neural information processing systems*, vol. 28, 2015.
- [42] I. Goodfellow, J. Pouget-Abadie, M. Mirza, B. Xu, D. Warde-Farley, S. Ozair, A. Courville, and Y. Bengio, “Generative adversarial networks,” *Communications of the ACM*, vol. 63, no. 11, pp. 139–144, 2020.
- [43] C. Lu, Y. Zhou, F. Bao, J. Chen, C. Li, and J. Zhu, “Dpm-solver++: Fast solver for guided sampling of diffusion proba-

- bilistic models,” *Machine Intelligence Research*, pp. 1–22, 2025.
- [44] W. Zhao, L. Bai, Y. Rao, J. Zhou, and J. Lu, “Unipc: A unified predictor-corrector framework for fast sampling of diffusion models,” *Advances in Neural Information Processing Systems*, vol. 36, pp. 49 842–49 869, 2023.
- [45] D. Watson, J. Ho, M. Norouzi, and W. Chan, “Learning to efficiently sample from diffusion probabilistic models,” *arXiv preprint arXiv:2106.03802*, 2021.
- [46] Z. Lyu, X. Xu, C. Yang, D. Lin, and B. Dai, “Accelerating diffusion models via early stop of the diffusion process,” *arXiv preprint arXiv:2205.12524*, 2022.
- [47] H. Zheng, P. He, W. Chen, and M. Zhou, “Truncated diffusion probabilistic models,” *arXiv preprint arXiv:2202.09671*, vol. 1, no. 3.1, p. 2, 2022.
- [48] H. Zheng, W. Nie, A. Vahdat, K. Azizzadenesheli, and A. Anandkumar, “Fast sampling of diffusion models via operator learning,” in *International conference on machine learning*. PMLR, 2023, pp. 42 390–42 402.
- [49] T. Salimans and J. Ho, “Progressive distillation for fast sampling of diffusion models,” *arXiv preprint arXiv:2202.00512*, 2022.
- [50] C. Meng, R. Rombach, R. Gao, D. Kingma, S. Ermon, J. Ho, and T. Salimans, “On distillation of guided diffusion models,” in *Proceedings of the IEEE/CVF Conference on Computer Vision and Pattern Recognition*, 2023, pp. 14 297–14 306.
- [51] Y. Song and P. Dhariwal, “Improved techniques for training consistency models,” *arXiv preprint arXiv:2310.14189*, 2023.
- [52] Z. Geng, A. Pokle, W. Luo, J. Lin, and J. Z. Kolter, “Consistency models made easy,” *arXiv preprint arXiv:2406.14548*, 2024.
- [53] H. Liu, Q. Xie, T. Ye, Z. Deng, C. Chen, S. Tang, X. Fu, H. Lu, and Z.-J. Zha, “Scott: Accelerating diffusion models with stochastic consistency distillation,” in *Proceedings of the AAAI Conference on Artificial Intelligence*, vol. 39, no. 5, 2025, pp. 5451–5459.
- [54] S. Lee, Z. Lin, and G. Fanti, “Improving the training of rectified flows,” *Advances in neural information processing systems*, vol. 37, pp. 63 082–63 109, 2024.
- [55] X. Liu, C. Gong, and Q. Liu, “Flow straight and fast: Learning to generate and transfer data with rectified flow,” *arXiv preprint arXiv:2209.03003*, 2022.
- [56] X. Liu, X. Zhang, J. Ma, J. Peng *et al.*, “Instaflow: One step is enough for high-quality diffusion-based text-to-image generation,” in *The Twelfth International Conference on Learning Representations*, 2023.
- [57] T. Xu, P. Mi, R. Wang, and Y. Chen, “Towards faster training of diffusion models: An inspiration of a consistency phenomenon,” *arXiv preprint arXiv:2404.07946*, 2024.
- [58] P. Achlioptas, O. Diamanti, I. Mitliagkas, and L. Guibas, “Learning representations and generative models for 3d point clouds,” in *International conference on machine learning*. PMLR, 2018, pp. 40–49.
- [59] D. Valsesia, G. Fracastoro, and E. Magli, “Learning localized generative models for 3d point clouds via graph convolution,” in *International conference on learning representations*, 2018.
- [60] X. Liu, X. Kong, L. Liu, and K. Chiang, “Treedgan: syntax-aware sequence generation with generative adversarial networks,” in *2018 IEEE International Conference on Data Mining (ICDM)*. IEEE, 2018, pp. 1140–1145.
- [61] R. Gal, A. Bermano, H. Zhang, and D. Cohen-Or, “Mrgan: Multi-rooted 3d shape representation learning with unsupervised part disentanglement,” in *Proceedings of the IEEE/CVF International Conference on Computer Vision*, 2021, pp. 2039–2048.
- [62] B. Zhang, M. Nießner, and P. Wonka, “3dilig: Irregular latent grids for 3d generative modeling,” *Advances in Neural Information Processing Systems*, vol. 35, pp. 21 871–21 885, 2022.
- [63] Y. Li, Y. Dou, X. Chen, B. Ni, Y. Sun, Y. Liu, and F. Wang, “Generalized deep 3d shape prior via part-discretized diffusion process,” in *Proceedings of the IEEE/CVF Conference on Computer Vision and Pattern Recognition*, 2023, pp. 16 784–16 794.
- [64] Y.-C. Cheng, H.-Y. Lee, S. Tulyakov, A. G. Schwing, and L.-Y. Gui, “Sdfusion: Multimodal 3d shape completion, reconstruction, and generation,” in *Proceedings of the IEEE/CVF Conference on Computer Vision and Pattern Recognition*, 2023, pp. 4456–4465.
- [65] R. Cai, G. Yang, H. Averbuch-Elor, Z. Hao, S. Belongie, N. Snavely, and B. Hariharan, “Learning gradient fields for shape generation,” in *Computer Vision—ECCV 2020: 16th European Conference, Glasgow, UK, August 23–28, 2020, Proceedings, Part III 16*. Springer, 2020, pp. 364–381.
- [66] T. Kimura, T. Matsubara, and K. Uehara, “Chartpointflow for topology-aware 3d point cloud generation,” in *Proceedings of the 29th ACM International Conference on Multimedia*, 2021, pp. 1396–1404.
- [67] S. Li, M. Liu, and C. Walder, “Editvae: Unsupervised parts-aware controllable 3d point cloud shape generation,” in *Proceedings of the AAAI Conference on Artificial Intelligence*, vol. 36, no. 2, 2022, pp. 1386–1394.
- [68] Z. Liu, H. Tang, Y. Lin, and S. Han, “Point-voxel cnn for efficient 3d deep learning,” *Advances in neural information processing systems*, vol. 32, 2019.
- [69] J. L. Ba, “Layer normalization,” *arXiv preprint arXiv:1607.06450*, 2016.
- [70] A. X. Chang, T. Funkhouser, L. Guibas, P. Hanrahan, Q. Huang, Z. Li, S. Savarese, M. Savva, S. Song, H. Su *et al.*, “Shapenet: An information-rich 3d model repository,” *arXiv preprint arXiv:1512.03012*, 2015.
- [71] L. Zhou, Y. Du, and J. Wu, “3d shape generation and completion through point-voxel diffusion,” in *Proceedings of the IEEE/CVF international conference on computer vision*, 2021, pp. 5826–5835.
- [72] R. Li, X. Li, K.-H. Hui, and C.-W. Fu, “Sp-gan: Sphere-guided 3d shape generation and manipulation,” *ACM Transactions on Graphics (TOG)*, vol. 40, no. 4, pp. 1–12, 2021.
- [73] D. Zhang, C. Choi, J. Kim, and Y. M. Kim, “Learning to generate 3d shapes with generative cellular automata,” *arXiv preprint arXiv:2103.04130*, 2021.
- [74] L. Hui, R. Xu, J. Xie, J. Qian, and J. Yang, “Progressive point cloud deconvolution generation network,” in *Computer Vision—ECCV 2020: 16th European Conference, Glasgow, UK, August 23–28, 2020, Proceedings, Part XV 16*. Springer, 2020, pp. 397–413.
- [75] A. Paszke, S. Gross, F. Massa, A. Lerer, J. Bradbury, G. Chanan, T. Killeen, Z. Lin, N. Gimelshein, L. Antiga *et al.*, “Pytorch: An imperative style, high-performance deep learning library,” *Advances in neural information processing systems*, vol. 32, 2019.
- [76] D. P. Kingma, “Adam: A method for stochastic optimization,” *arXiv preprint arXiv:1412.6980*, 2014.
- [77] A. Vahdat, K. Kreis, and J. Kautz, “Score-based generative modeling in latent space,” *Advances in neural information processing systems*, vol. 34, pp. 11 287–11 302, 2021.
- [78] J. Kim, J. Yoo, J. Lee, and S. Hong, “Setvae: Learning hierarchical composition for generative modeling of set-structured data,” in *Proceedings of the IEEE/CVF Conference on Computer Vision and Pattern Recognition*, 2021, pp. 15 059–15 068.
- [79] Z. Liu, Y. Feng, M. J. Black, D. Nowrouzezahrai, L. Paull, and W. Liu, “Meshdiffusion: Score-based generative 3d mesh modeling,” *arXiv preprint arXiv:2303.08133*, 2023.
- [80] H. Zhao, L. Jiang, J. Jia, P. H. Torr, and V. Koltun, “Point transformer,” in *Proceedings of the IEEE/CVF international conference on computer vision*, 2021, pp. 16 259–16 268.
- [81] X. Wu, Y. Lao, L. Jiang, X. Liu, and H. Zhao, “Point transformer v2: Grouped vector attention and partition-based pooling,” *Advances in Neural Information Processing Systems*, vol. 35, pp. 33 330–33 342, 2022.
- [82] X. Lai, J. Liu, L. Jiang, L. Wang, H. Zhao, S. Liu, X. Qi, and J. Jia, “Stratified transformer for 3d point cloud segmentation,” in *Proceedings of the IEEE/CVF conference on computer vision and pattern recognition*, 2022, pp. 8500–8509.

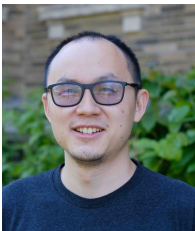


**Bi'an Du** received the B.S. degree in Artificial Intelligence from Peking University in 2022. He is currently working toward the Ph.D. degree at Wangxuan Institute of Computer Technology of Peking University. His research interests include 3D computer vision, generative models, etc.



**Wei Hu** (M'17-SM'21) received the B.S. degree in Electrical Engineering from the University of Science and Technology of China in 2010, and the Ph.D. degree in Electronic and Computer Engineering from the Hong Kong University of Science and Technology in 2015. She was a Researcher with Technicolor, Rennes, France, from 2015 to 2017. She is currently an Associate Professor with Wangxuan Institute of Computer Technology, Peking University. Her research interests are graph signal processing, graph-based machine learning and 3D

visual computing. She has authored around 90 international journal and conference publications, with several paper awards including Best Paper Candidate in CVPR 2021 and Best Student Paper Runner Up Award in ICME 2020. She was awarded the 2021 IEEE Multimedia Rising Star Award—Honorable Mention, and the 2023 Outstanding Editorial Board Member Award in IEEE Signal Processing Society. She serves as an Associate Editor for IEEE Signal Processing Magazine and IEEE Transactions on Signal and Information Processing over Networks. She serves as TPC Co-Chair for ICME 2026, Special Session Co-Chair for ICME 2025, etc.



**Renjie Liao** is an Assistant Professor in the Department of Electrical and Computer Engineering and an Associate Member of the Department of Computer Science at the University of British Columbia (UBC). He is also a faculty member at the Vector Institute and holds a Canada CIFAR AI Chair. Prior to joining UBC, he was a Visiting Faculty Researcher at Google Brain. He received his Ph.D. in Computer Science from the University of Toronto in 2021. During his Ph.D., he also worked as a Senior Research Scientist at Uber Advanced Technologies

Group. He holds an M.Phil. in Computer Science from the Chinese University of Hong Kong (2015) and a B.Eng. in Automation from Beihang University (2011). His research interests span machine learning and its intersection with computer vision, self-driving, healthcare, and beyond, with a particular focus on probabilistic and geometric deep learning.